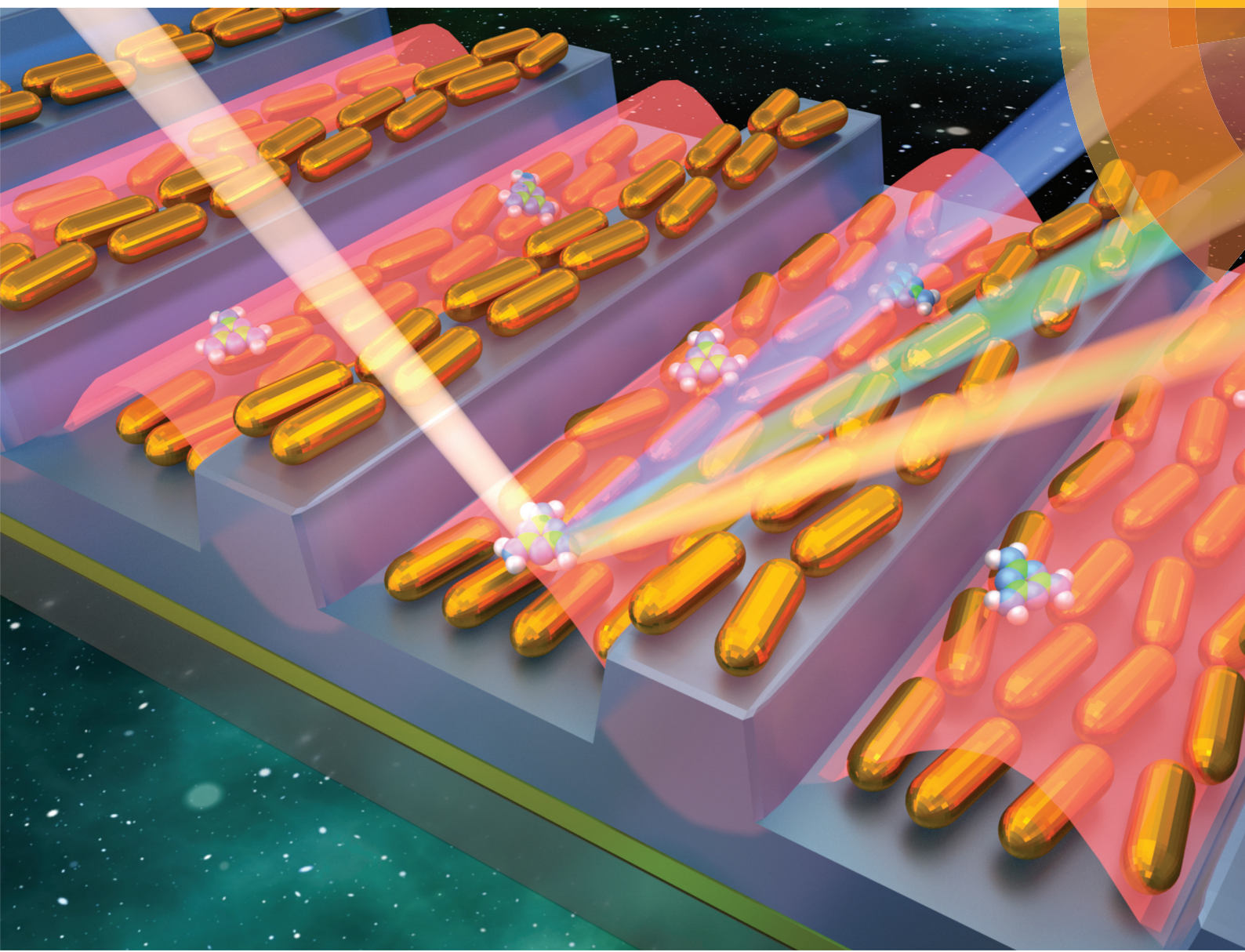


Nanoscale

rsc.li/nanoscale



ISSN 2040-3372



ROYAL SOCIETY
OF CHEMISTRY

Celebrating
IYPT 2019

PAPER

Yang Shen, Chongjun Jin et al.

Surface-enhanced Raman scattering induced by the coupling of the guided mode with localized surface plasmon resonances



NCNST

Cite this: *Nanoscale*, 2019, **11**, 14164

Surface-enhanced Raman scattering induced by the coupling of the guided mode with localized surface plasmon resonances[†]

Shaoying Wu,^{a,b} Yang Shen^{*a} and Chongjun Jin  ^{*a}

Surface-enhanced Raman spectroscopy (SERS) is considered to be a powerful analysis tool for the detection of molecules due to its ultra-high sensitivity and non-destructive nature. Here, we introduce a new type of hybrid SERS substrate, where gold nanorods are assembled on a structured support containing a top dielectric grating, dielectric spacer and gold mirror. Compared with the conventional metal nanoparticle assemblies on a flat support, our hybrid substrate shows an approximately 30-fold enhancement in the SERS signal. Numerical simulations show that such a substantial boost arises from the amplification of the absorption cross sections of the gold nanorods and the heating of the "hot spots" around the gold nanorods by the coupling between the guided mode in the structured support and the localized surface plasmon resonances. This mode coupling can be easily tuned by changing the thickness of the spacer. In addition, this substrate also presents uniform spot-to-spot and sample-to-sample SERS signals of the analyte molecules (relative standard deviations down to 7.4% and 6.1%, respectively). Moreover, the performance of this substrate has been demonstrated with the detection of melamine and cytosine, suggesting its great potential in food safety regulation and bioassays. This grating-mirror-enhanced strategy is available to any other SERS-active nanoparticles synthesized by chemical methods, which might offer new opportunities for improving the performance of the chemically prepared nanoparticles in realistic SERS-related applications.

Received 2nd April 2019,

Accepted 12th June 2019

DOI: 10.1039/c9nr02831e

rsc.li/nanoscale

Introduction

Surface-enhanced Raman scattering is a non-destructive and ultrasensitive spectroscopy technique for identifying trace analytes and enables many applications, including food safety regulation,^{1,2} environmental monitoring,^{3,4} and DNA analysis.^{5,6} A giant signal enhancement, a highly uniform and reproducible response, and an easy fabrication method are required for an ideal SERS substrate. After several decades of intensive research on SERS, the enhancement mechanism of SERS has been ascribed to a combination of the electromagnetic enhancement, which is proportional to the fourth power of the local electric field intensity,⁷ and the chemical enhancement, which is related to the charge-transfer effect between

the SERS substrate and the analytes.⁸ Generally, the electromagnetic enhancement plays a more important role in SERS, therefore most of the studies on SERS substrates are focused on the maximization of electromagnetic field intensity. The localized surface plasmon resonances (LSPRs) of metallic nanostructures are generally used to generate a high local electromagnetic field in their nanoscale region. For instance, the colloids of metallic nanoparticles that contain sharp edges, sharp spikes or deep gaps including nano-flower,⁹ nano-dumbbell,¹⁰ nano-snowmen,¹¹ nano-urchins,¹² and silver particles with concave surfaces¹³ have been demonstrated as efficient SERS-active substrates. However, these chemically prepared nanoparticles always suffer from a poor reproducibility due to the variability in their particle distances, sizes, orientations, and morphologies.¹⁴ In contrast, the high-resolution fabrication techniques including electron beam lithography and focused ion beam milling can control the shape, size, and gap distance of the nanoparticles precisely,¹⁵ thereby enabling an extremely strong electric field at the specific position and a better reproducibility. Unfortunately, these precise fabrication methods are expensive and time consuming, preventing their widespread use in realistic applications. In addition, such lithographically prepared substrates are also limited by a low

^aState Key Laboratory of Optoelectronic Materials and Technologies, School of Materials Science and Engineering, Sun Yat-sen University, Guangzhou 510275, China. E-mail: jinchjun@mail.sysu.edu.cn, sheny@mail2.sysu.edu.cn

^bSchool of Electronics and Information Technology, Sun Yat-sen University, Guangzhou 510275, China

[†] Electronic supplementary information (ESI) available. See DOI: 10.1039/c9nr02831e

density of hot spots due to the nature of the fabrication methods, dramatically lowering their performance for detecting trace molecules at ultralow concentrations.

Recently, the hybridization strategy by integrating the nanoparticles with the surrounding nanostructures or patterned substrates has been demonstrated as an efficient method to enhance the SERS performance of the nanoparticles.^{14,16–20} For instance, adding gold strips and gold reflectors can simultaneously improve the local field enhancement and SERS collection efficiency of optical antennas.¹⁶ Integrated with an external ring cavity, the SERS performance of an Au/Ag nano-star dimer was also improved.¹⁸ Self-assembly of nanoparticles into close-packed arrays at patterned substrates is another approach to generate high-performance SERS substrates.^{19,20} A substrate of grating-integrated gold nanograsses enables an ultrasensitive, uniform and reproducible SERS detection due to the formation of high-density enhanced hot-spots.¹⁹

In this work, we show a novel SERS substrate, where the gold nanorods (GNRs) are placed on the grating-dielectric spacer-mirror substrate (GDMS). In this hybrid system, besides the direct excitation of LSPRs of the GNRs, the leaking energy of the guided mode is coupled or recoupled to the LSPRs by the reflection of the underneath gold mirror. The recycling of the energy will lead to further amplification of the local electric field in the affinity of GNRs. With this effect of the GDMS, GNRs placed on the GDMS (GNRs-GDMS) experimentally shows a SERS enhancement factor of 30 higher than that for the GNRs placed on a flat polymer substrate when Rhodamine 6G molecules were adsorbed. Furthermore, we also demonstrate the benefit of the GNRs-GDMS with the detection of dyes, DNA bases and food additives, respectively, suggesting that this substrate is a promising candidate for the practical SERS detection.

Results and discussion

Optical properties of GNRs-GDMS

Guided mode resonators (GMRs), consisting of a dielectric grating and a waveguide layer with a high permittivity material, have a distinct enhancement effect on the LSPRs, thus they have been employed in the architecture of SERS substrates^{21,22} and other sensors.²³ Here, we demonstrate this guided mode-enhanced idea with the GDMS to boost the LSPRs of the GNRs. Fig. 1 is the schematic illustration showing the configuration of the GNRs-GDMS. The GDMS, composed of a polystyrene (PS) grating, PS spacer, and gold mirror, acts as a GMR which enhances the coupling of LSPRs of GNRs with the incident light. The optically thick gold film reflects the transmitted light effectively to reduce the energy leakage passing through the substrate. As the generators of hot spots for the SERS substrates, the GNRs are arranged randomly on the GDMS. According to the aforementioned design concept, the GNRs will provide a considerable number of hot-spots to ensure their SERS performance. Meanwhile, the GDMS will further strengthen these hot-spots through the guided mode and reflection by the gold mirror.

To investigate the optical properties of the GNRs-GDMS and the enhancement mechanism, we employed the finite-difference-time-domain (FDTD) method (FDTD Solutions, Lumerical) to simulate the corresponding absorption spectra and the local electric intensity distributions of GNRs-GDMS. In the simulations, all the samples were excited by a normally incident light with an electric field parallel to the grating stripes. More details about the simulation can be found in the ESI.† For discussion, we defined the absorption as $A = 1 - T - R$ (where, T and R refer to the transmission and reflection of the samples, respectively), and the absorption spectra are recorded

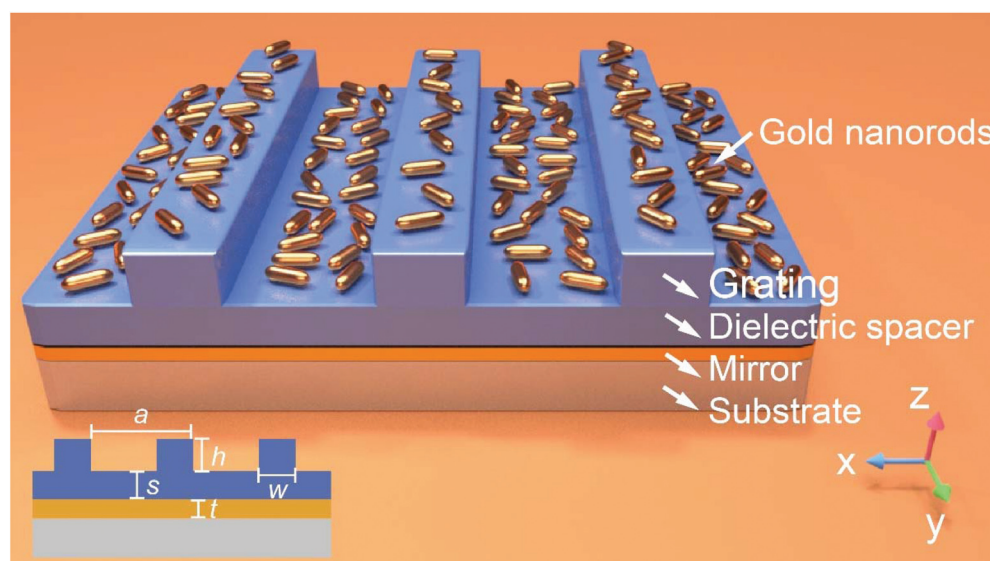


Fig. 1 Schematic illustration of a GNRs-GDMS. (Inset) The geometric parameters of the structure. a and h represent the period and height of the PS grating. w represents the width of the PS grating stripe. s represents the thickness of the PS spacer. The thickness of the mirror is fixed at $t = 100$ nm.

by calculating/measuring the corresponding transmission and reflection spectra.

In Fig. 2, we present the simulated absorption spectra and local electric field distributions of a GNRs-GDMS and its counterparts to reveal the effect of the GDMS on GNRs. Fig. 2a shows the absorption spectrum of the GNRs (length $l = 70$ nm and diameter $d = 32$ nm) randomly arranged on the PS film, where a broad and weak peak P1' appears at $\lambda = 658$ nm. The electric field is mainly concentrated at the edges of the nanorods (Fig. 2a) at the P1' peak, indicating that this absorption peak is dominated by the LSPRs of the GNRs. It should be noted that the arrangement of the GNRs has almost no distinct effect on the overall optical properties (the simulated absorption spectra of the GNRs-GDMS with different arrangements of GNRs can be seen in Fig. S1, ESI†). When integrated with a GDMS ($a = 500$ nm, $s = 160$ nm, $h = 200$ nm, $w = 167$ nm), the GNRs with the same parameters show a significantly enhanced absorption peak P1 at $\lambda = 633$ nm. The corresponding electric field exhibits a 4-fold enhancement around the individual gold nanorods compared to that of the GNRs on the PS film (Fig. 2b). The periodic electric field pattern along the x -direction in the right subgraph of Fig. 2b suggests the hybridization of the LSPRs and guided mode (it is further con-

firmed by the cross-sectional electric field E_y and magnetic field H_z distributions in Fig. S2a and b, ESI†). This coupling effect can be understood that as the LSPR and guided mode spectrally overlap, the excited guided mode will be recoupled to and finally strengthens the LSPRs. Besides P1, the spectrum of GNRs-GDMS also exhibits another absorption peak P2 with a narrow linewidth at $\lambda = 500$ nm. This peak is attributed to Wood's anomaly in the air, namely, the in-plane diffraction caused by the grating, which is confirmed by the periodically patterned electric field above the GNRs-GDMS presented in Fig. S2c, ESI†. Moreover, we investigated the independent effects of the building blocks of the GDMS, the mirror and the dielectric grating, on the GNRs. Fig. 2c shows the absorption spectrum and the electric field intensity distribution of a structure composed of a PS spacer on a gold back mirror, which serves as a Fabry-Pérot cavity (FPC).^{24,25} It's clear that the combination of the GNRs and the FPC leads to a strong absorption peak P1'' and the local electric field is also enhanced (Fig. 2c). However, the electric field enhancement of GNRs-FPC is limited, because the electric field was largely concentrated within the FPC (Fig. S3, ESI†) and rarely extended to the GNR layer above the cavity. Fig. 2d depicts the absorption spectrum of a structure containing the GNRs on a dielectric grating

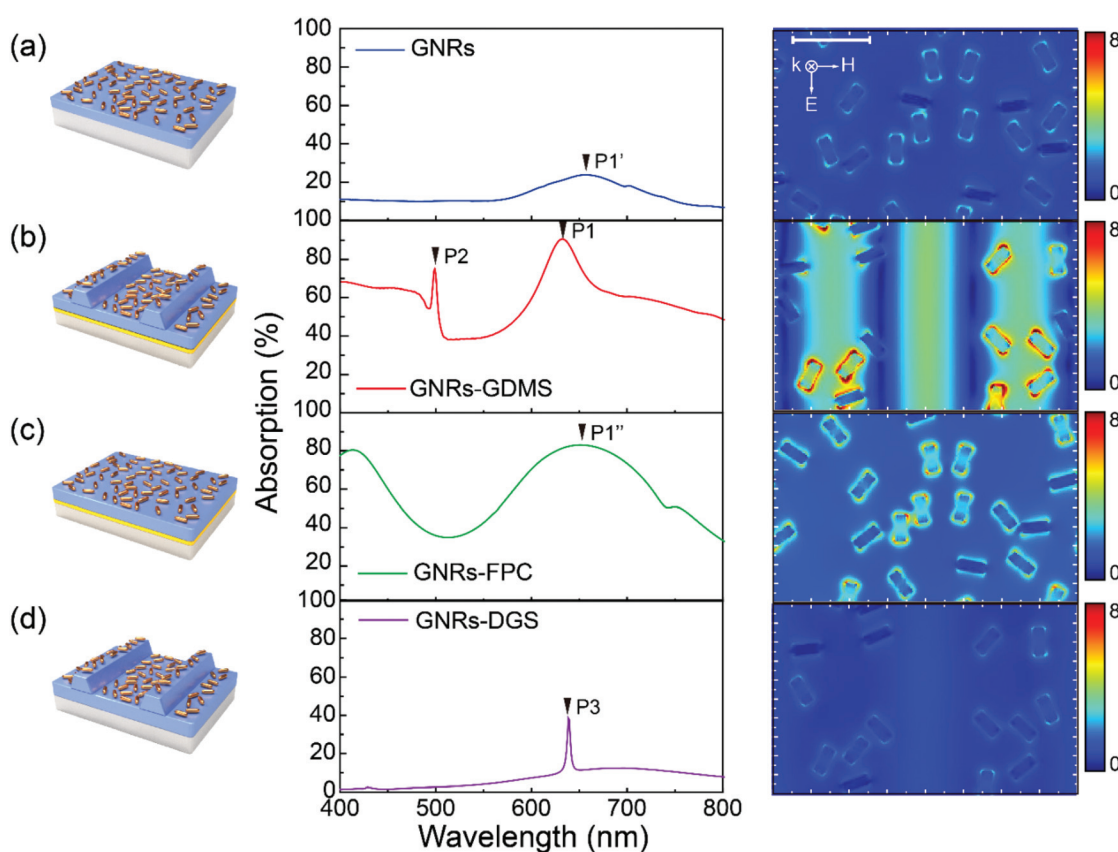


Fig. 2 Structure sketch (left), simulated absorption spectra (middle) and simulated electric field intensity distributions at 633 nm (right) of the GNRs placed on a PS film (a), GNRs-GDMS (b), GNRs-FPC (c) and GNRs-DGS (d). The scale bar in (a) is set to be 200 nm. The location of the electric field intensity distribution is 8 nm above the interface of PS and air.

and spacer (GNRs-GDMS). A guided mode is observed, which features a narrow absorption peak P3 at $\lambda = 633$ nm. Apparently, no enhancement in the electric field around the GNRs occurs (Fig. 2d) when compared to the pure GNRs placed on the PS film (Fig. 2a). This is explained by the energy leakage of the guided mode into the substrate in the absence of the back reflector (Fig. S4a–c, ESI†). The above results reveal that the boost on the absorption and hot spots depends on the synergistic effect of the F-P cavity and guided mode resonator, thus GNRs-GDMS is an optimal structure. It should be noted that we also simulated the absorption spectrum and the related electric field distributions of a GNRs-GDMS when the light is polarized perpendicularly to the grating and did not find any strong resonances. Therefore, we believe that the absorption and electric field enhancement under this polarization are not suitable for SERS applications. The simulated absorption spectrum and electric field distributions of a GNRs-GDMS as the polarization which is perpendicular to the grating can be found in Fig. S5, ESI.†

Preparation of GNRs-GDMS

To verify our design concept, we fabricated the GNRs-GDMS through a low-cost and high-throughput method as depicted in Fig. 3a. Briefly, two-beam interference lithography is firstly employed to pattern a grating of photoresist stripes on a quartz substrate as a master. Then, the pattern was transferred onto the PDMS by soft lithography to form a PDMS stamp with the complementary structure. To generate the base of the GDMS, 10 nm titanium and 100 nm gold were subsequently deposited on a quartz substrate by magnetron sputtering, followed by the spin-coating of a PS layer. After that, the patterned PDMS stamp was imprinted onto the as-prepared PS film under uniaxial compression at an increased temperature. After cooling, the PDMS mold was removed to form the GDMS. The surface of the GDMS was modified by oxygen plasma treatment to make it negatively charged. Finally, the GDMS was covered by a certain amount of positively charged GNR aqueous solution, during which the GNRs adhered to the sub-

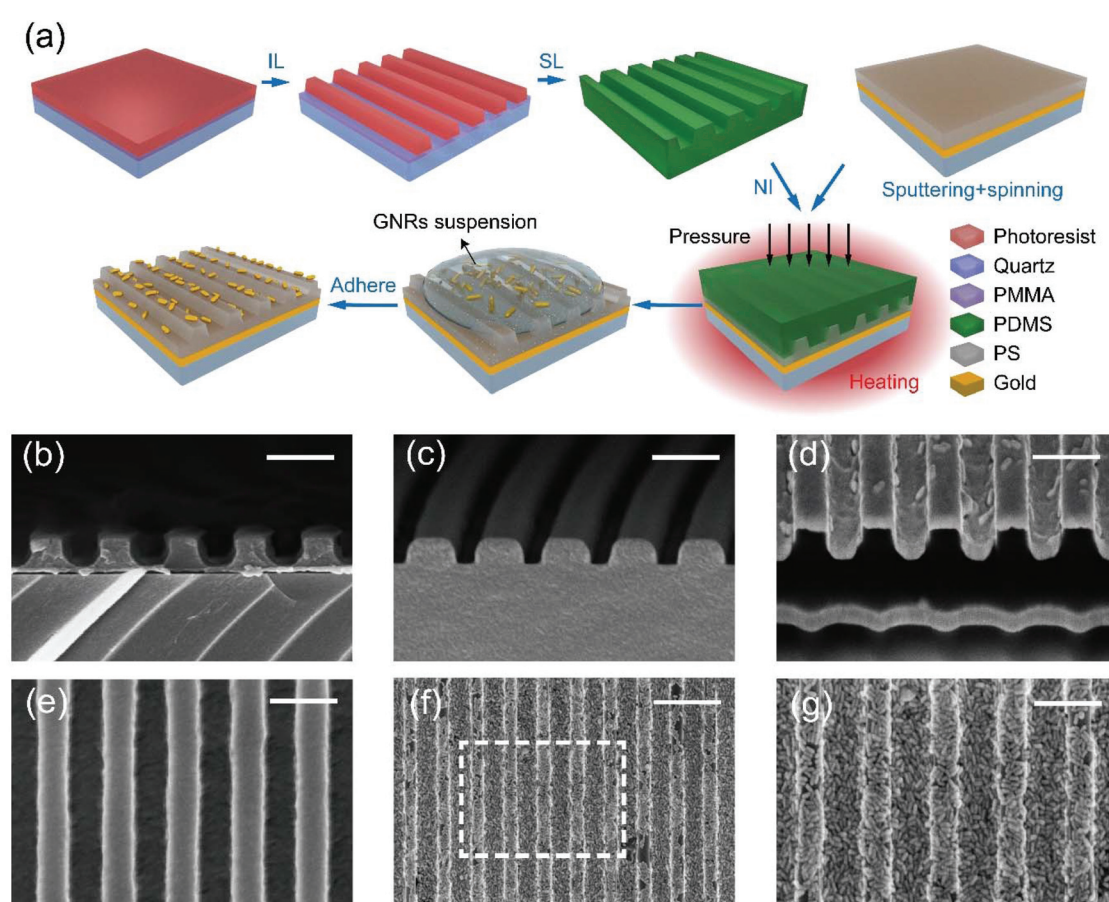


Fig. 3 (a) Fabrication scheme of GNRs-GDMS. IL, SL, and NI stand for interference lithography, soft lithography and nano-imprint, respectively. (b) Cross-sectional SEM image of a grating formed in photoresist (lattice constant $a = 500$ nm and stripe height $h = 220$ nm). (c) Cross-sectional SEM image of a PDMS grating ($a = 500$ nm and $h = 200$ nm). (d) Cross-sectional SEM image of a PS grating on a PS layer and gold mirror. (e) Top-view SEM image of a PS grating on a PS layer and gold mirror. (f) Top-view SEM image of a GNRs-GDMS ($a = 500$ nm). The length and diameter of GNRs are 75 ± 15 nm and 31 ± 7 nm, respectively. (g) Top-view magnified SEM image of the GNRs-GDMS ($a = 500$ nm) in the region indicated with the dashed box in (f). Scale bars: (b–e, g) 500 nm; (f) 1 μ m.

strate by the electrostatic force. As the solvent evaporated, we obtained the resultant GNRs-GDMS. The detailed fabrication procedure could be found in the experimental section. More details about the preparation of the GNRs-GDMS are included in the experimental section.

Fig. 3b and c show the cross-sectional scanning electron microscopy (SEM) images of the photoresist grating on a quartz substrate fabricated by interference lithography and the PDMS stamp with a complementary grating obtained by soft-lithography. The periods of the grating structures were 500 nm. The height of the PDMS grating was 200 nm, which was a little lower than that of the photoresist grating (220 nm). This could be attributed to the volume shrinkage of the PDMS stamp in the soft-lithography process. Fig. 3d shows the FIB-milled cross-sectional SEM image of the GDMS with a distinct layered structure fabricated by nanoimprinting, which consists of a PS grating, a PS spacer (the dark part under the grating), and a gold mirror (the bright part under the spacer). Fig. 3e and f show the top-view SEM images of a GDMS before and after the assembly of GNRs, respectively. Fig. 3g shows a top-view magnified SEM image of a GNRs-GDMS. From Fig. 3f and g, the surface of the GDMS was covered by a monolayer of GNRs, and the periodic brightness change in the direction perpendicular to the grating indicated that the grating structure was not destroyed in the adhesion process of GNRs. The length and the diameter of the GNRs were 75 ± 15 nm and 31 ± 7 nm, and the density is 376 ± 13 nanorods per μm^2 as obtained from the top-view SEM images of GNRs-GDMS.

To optimize the performance of GNRs-GDMS as a SERS substrate and investigate the interaction mechanism between the guided mode and LSPR, multiple samples with different spacer thicknesses s were fabricated. We measured the absorption spectra of GNRs-GDMS with varying s from 170 nm to 330 nm under a normally incident light, whose electric field was parallel to the grating stripes. By controlling s , the resonance wavelength of the guided mode induced by the GDMS can be flexibly tuned, which can be found in Fig. S6a in the ESI.[†] As shown in Fig. 4a, with the increase in the thickness, the absorption peak P1 redshifts and its intensity first rises and then falls concomitantly (these trends agree reasonably well with the simulated spacer-thickness-modulated absorption spectra in Fig. S7, ESI[†]). In particular, for $s = 170$ nm to 230 nm, the absorption intensity of P1 keeps rising from 86% to 92%, which is explained by the spectral overlap of the guided mode and the LSPRs from the GNRs according to our previous analysis (the absorption spectra of the GDMS and the GNRs placed on the PS film are depicted in Fig. S6a and b, ESI[†]). The guided mode resonance wavelengths of the GDMSs with the spacers of 200 nm (648 nm) and 230 nm (658 nm) are close to the LSPR wavelength of the GNRs (651 nm), thus it leads to stronger absorptions. As the thickness further increases, P1 shows a sudden decrease in intensity, which is attributed to the detuning between the guided mode and the LSPRs. In addition, we also checked the influences of period a and height h of the grating on the absorption spectra of GNRs-GDMSs. Considering the match of the resonance wavelength

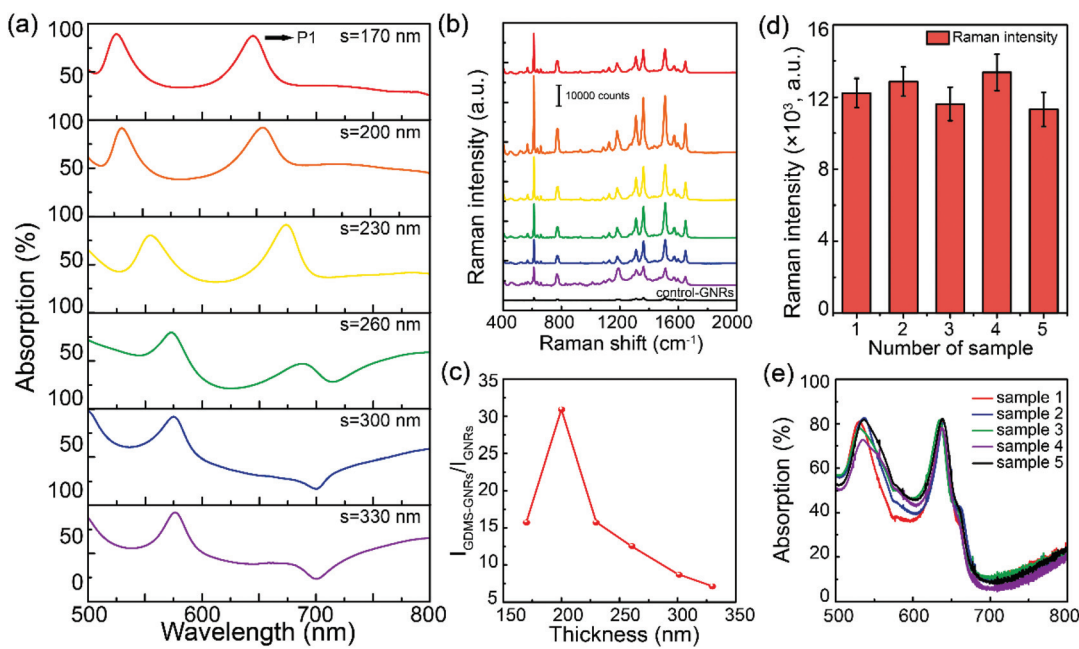


Fig. 4 (a) Measured absorption spectra of GNRs-GDMSs ($a = 500$ nm, $h = 200$ nm, $t = 100$ nm) with various spacer thicknesses, $s = 170, 200, 230, 260, 300$, and 330 nm. (b) Measured Raman spectra of Rhodamine 6G on GNRs-GDMS with different s . (c) Raman intensity ratio of 10^{-6} M R6G on GNRs-GDMS and that on GNRs at the 612 cm^{-1} band as a function of spacer thickness. (d) Raman intensities of 10^{-6} M R6G on five GNRs-GDMS samples. The error bars indicate the relative standard deviations which were determined by the measurements at three random spots for each sample. (e) Absorption spectra of these five GNRs-GDMS samples. For the GNRs-GDMSs used in these experiments, the gold nanorods were assembled on a dense monolayer on the surface of the GDMS.

to the excitation laser line of 633 nm and the yield requirement in fabrication procedures, the optimal period and height of the grating was determined to be $a = 500$ nm and $h = 200$ nm, respectively (simulated period-modulated and grating-height-modulated absorption spectra can be seen in Fig. S8, ESI[†]).

To affirm the GDMS-induced SERS enhancement, we examined the Raman spectra of Rhodamine 6G (R6G) molecules adsorbed onto the GNRs-GDMS samples with different thicknesses of the spacer, as shown in Fig. 4b. These samples were soaked in the R6G aqueous solution (10^{-6} M) for 1 hour, then washed with deionized water several times, and finally dried under a nitrogen flow. All the Raman signals were acquired using a Raman spectrometer (LabRAM HR, HORIBA Scientific) with a 633 nm excitation laser. More details about the Raman measurements are presented in the Experimental Section. In the Raman spectra, the characteristic vibration bands of R6G are visible, including the C-C-C deformation in-plane vibration at 614 cm^{-1} , the out-of-plane vibration of the deformed C-H bond at 775 cm^{-1} , the in-plane vibration of the

deformed C-H bonds at 1187 cm^{-1} , the C-C stretching modes at 1313 cm^{-1} , 1361 cm^{-1} , 1512 cm^{-1} , and 1649 cm^{-1} , and the C-O-C bond stretching vibration at 1573 cm^{-1} , respectively.^{26,27} As a control group, the Raman spectrum of R6G adsorbed onto a substrate containing a flat PS layer covered by GNRs was also examined, where the sample was under the same molecular adsorption and measurement conditions (black curve, Fig. 4b). Here, we define the structure-induced Raman enhancement factor as $I_{\text{GDMS-GNRs}}/I_{\text{GNRs}}$, namely, the Raman intensity ratio acquired from the GNRs-GDMS to the control group. According to the definition, the dependence of the structure-induced Raman enhancement factor on the spacer thickness is presented in Fig. 4c. Note that with the increase in the spacer thickness, the Raman intensity of the GNRs-GDMS rises first and then falls, which is similar to the effect of the spacer thickness on the optical absorption. Particularly, as for $s = 200$ nm, the GNRs-GDMS sample achieves the highest Raman enhancement factor up to 30 at 612 cm^{-1} . It should be noticed that the Raman signal of R6G from the GNRs-GDMS with $s = 200$ nm is stronger than

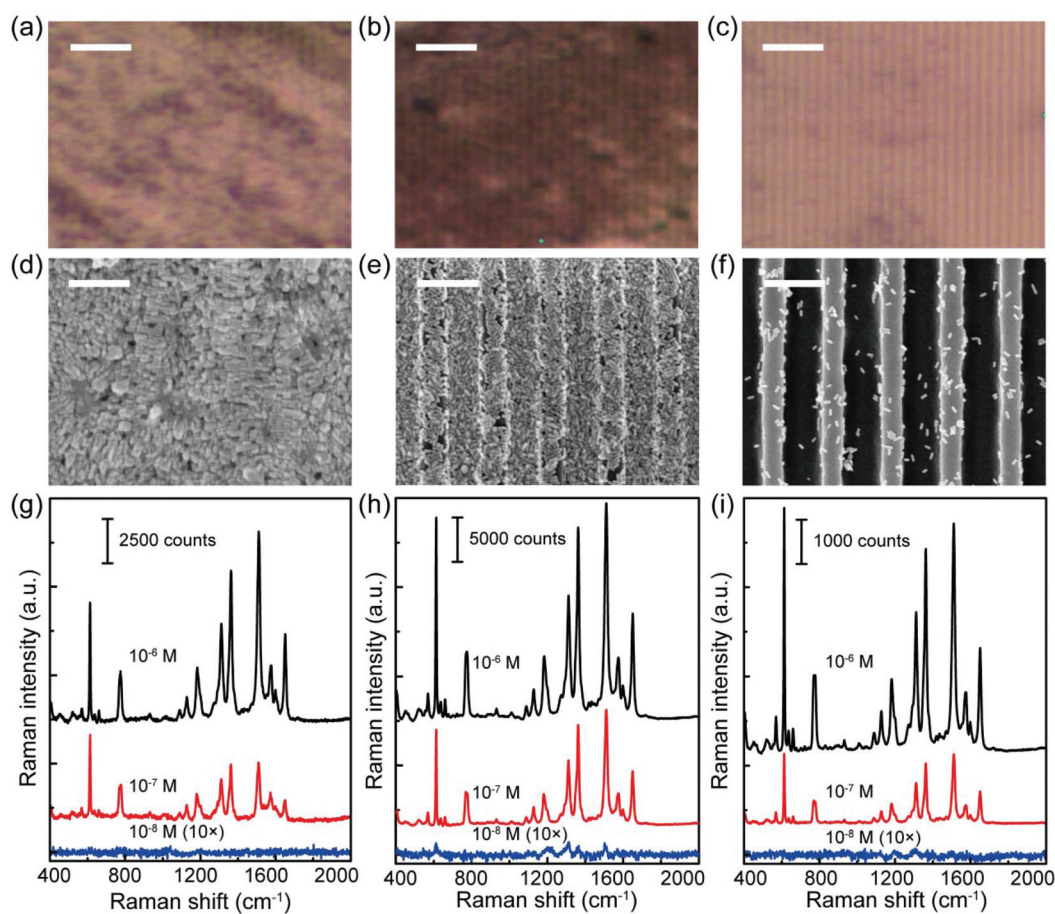


Fig. 5 Influence of the density of nanorods on the overall SERS performance of GNRs-GDMS. (a–c) Optical micrographs of three samples with different densities of gold nanorods: multilayer, monolayer and sparse GNRs arrangements. (d–f) SEM images of these three samples with different densities of gold nanorods. (g–i) Raman spectra acquired from these three kinds of samples treated by the R6G solutions with different concentrations from 10^{-6} M to 10^{-8} M. The other parameters of all GNRs-GDMSs are $a = 500$ nm, $h = 200$ nm, $s = 200$ nm, and $t = 100$ nm. Scale bars: (a–c) $3\text{ }\mu\text{m}$; (d–f) 500 nm .

that from the GNRs-GDMS with $s = 230$ nm, though the latter has a stronger absorption peak. This can be explained by the theory that the SERS enhancement is optimal when the maximum extinction product of an excitation and the corresponding Raman scattering wavelengths is achieved.²⁸ This result not only reveals the correlation between the SERS performance and detuning between the guided mode and LSPRs, but also indicates the importance of an excitation wavelength, in terms of engineering the SERS systems for optimum performance.

In addition, we also estimated the general average SERS enhancement factor (EF) of the GNRs-GDMS treated by 10^{-7} M R6G solution according to the following equation¹⁵

$$\text{EF} = \frac{I_{\text{SERS}}}{I_{\text{RS}}} \times \frac{N_{\text{RS}}}{N_{\text{SERS}}} \times \frac{P_{\text{RS}}}{P_{\text{SERS}}} \times \frac{t_{\text{RS}}}{t_{\text{SERS}}}.$$

The calculated EFs at the main peaks of 614, 775, 1313, 1361, 1512 and 1649 cm^{-1} are shown in Table S1, ESI.† The highest EF of 1.82×10^6 is achieved at 1649 cm^{-1} . (More details on the EF calculation are shown in the ESI.†) This value is one order of magnitude higher than the reported ones in the literature for the assembled metal nanoparticles and nanowires systems on planar substrates,^{29–31} suggesting the enhancement effect caused by our structured substrate.

We also investigated the reproducibility of GNRs-GDMSs in terms of spot-to-spot and sample-to-sample Raman intensity variations. Five samples were fabricated under the same conditions. The spectral position of P1 varies within 5 nm (Fig. 4e) among the different samples and the small spot-to-

spot and sample-to-sample relative standard deviations of 7.4% and 6.1% were achieved (Fig. 4d).

Due to the presence of strong plasmon coupling between the adjacent gold nanorods, the density of nanorods also plays a key role in the SERS performance of GNRs-GDMS. To optimize the density of the nanorods, we fabricated the three types of GNRs-GDMS samples with different densities of the nanorods. Fig. 5a–c and d–f show the optical micrographs and SEM images of these three configurations: multilayer, monolayer and sparse GNR arrangements. For R6G detection (10^{-6} M to 10^{-8} M), the highest SERS intensities occur in the monolayer nanorod arrangement (Fig. 5h). This high intensity benefits from the strong coupling between the nanorods and the GDMS-induced SERS enhancement. However, the SERS intensities of the multilayer nanorod arrangement are lower than those of the monolayer nanorod arrangement (Fig. 5g) even though it has a higher density of nanorods. It can be ascribed to the attenuation of the guide mode as the grating is planarized by multilayer nanorods (Fig. 5a and d). In addition, the sparse nanorod arrangement shows the weakest SERS signals (Fig. 5i) due to the limited amount of nanorods (Fig. 5f) and the lack of nanorod coupling.

Application of GNRs-GDMS

Based on the low-cost preparation and the relatively high SERS enhancement of GNRs-GDMS, we demonstrate its applicability in practical use. Several molecules including malachite green, melamine and cytosine were used as analytes.

Malachite green is a water-soluble dye and has been widely used in aquaculture for reducing parasite and fungal infection

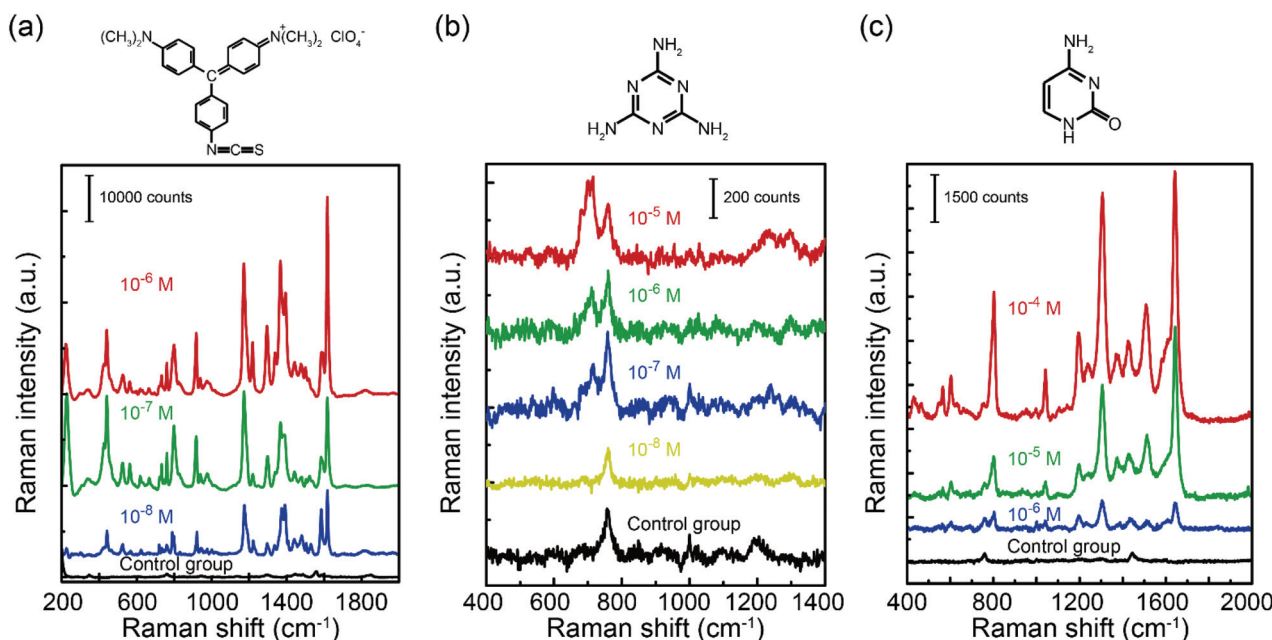


Fig. 6 Raman spectra acquired from GNRs-GDMS ($a = 500$ nm, $h = 200$ nm, $s = 200$ nm, and $t = 100$ nm) treated with the solutions of different analytes with different concentrations. (a) MGITC (10^{-6} – 10^{-8} M). (b) Melamine (10^{-5} – 10^{-8} M). (c) Cytosine (10^{-4} – 10^{-6} M). The control groups are treated with ultrapure water. The subgraphs are the structural formulae of MGITC, melamine and cytosine. For the GNRs-GDMSs used in these experiments, the gold nanorods were assembled on a dense monolayer on the surface of GDMS.

in fish.³² However, it was harmful to human beings because of its mutagenic and teratogenic effects. In our experiment, we obtained the Raman signal from multiple samples with identical geometrical parameters ($a = 500$ nm, $h = 200$ nm, $s = 200$ nm, $t = 100$ nm) treated with a series of malachite green isothiocyanate (MGITC) aqueous solutions with different concentrations from 10^{-6} to 10^{-8} M. Fig. 6a shows the corresponding Raman spectra. The typical peaks at 1180 cm^{-1} , 1367 cm^{-1} , 1392 cm^{-1} , and 1618 cm^{-1} are related to the in-plane benzene ν_9 mode, phenyl–N stretching, in-plane C–C and C–H stretching and phenyl–N + C–C stretching mode, respectively.³³ The detection limit of the MGITC is about 10 nM for GNRs-GDMS.

Melamine, an industrial material, has been illegally used as a food additive. The combination of melamine and its analogues, such as cyanuric acid, can result in kidney failures and even infant death.^{34,35} The limit of the melamine contained in infant food is set to be 1 mg L^{-1} (about 8×10^{-6} M) by the Codex Alimentarius Commission. To investigate the feasibility of GNRs-GDMS in the detection of the melamine in food, we measured the Raman spectra of multiple samples with identical geometrical parameters treated with melamine aqueous solutions with concentrations ranging from 10^{-5} to 10^{-8} M and presented in Fig. 6b. The characteristic Raman mode at 715 cm^{-1} (the ring-breathing II mode) was assigned to the in-plane deformation of the triazine ring.³⁶ The detection limit of the melamine is determined to be 10^{-7} M, which is superior to the solitary gold nanoparticle aggregate^{37,38} or silver nanoparticle array.³⁹ Such a lower detection limit can be attributed to the interplay between GDMS and GNRs. In addition, this detection limit was lower than the content limitation of the melamine in infant food. That's to say, the GNRs-GDMS has the potential to detect harmful additives in food, such as the melamine.

To further explore its potential in biological sensing, we used cytosine as the analyte. The cytosine is a part of nucleotides and one of the four main DNA bases. The identification of DNA bases is important to biological research including DNA sequencing.⁴⁰ In this work, we treated the GNRs-GDMS with cytosine aqueous solutions with different concentrations (10^{-4} – 10^{-6} M). Fig. 6c shows the SERS spectra recorded from multiple samples with identical geometry parameters. The typical Raman modes of cytosine are located at 796 cm^{-1} , 1302 cm^{-1} and, 1643 cm^{-1} , which are related to the ring-breathing mode, (C–NH₂) + in-plane (ring) mode and in-plane $\delta(\text{NH}_2)$ mode, respectively.⁴¹ These modes are visible for the concentration of 10^{-6} M.

Conclusions

In summary, we have developed a hybrid substrate consisting of a dielectric grating, a dielectric layer, and a gold mirror for improving the SERS performance of gold nanorods. We have experimentally fabricated such GNRs-GDMS and demonstrated an amplification of the SERS signal by a factor of 30 compared

to that of gold nanorods placed on a planar dielectric substrate. FDTD simulations and the control experiment reveal that the interaction of the guided mode and the LSPR is the main reason for enhancing the SERS performance of these nanoparticles. In addition, the recycling of the leaked energy from the guided mode would boost the local electric field intensity around the particles and lead to a higher SERS enhancement factor. In the meantime, the relative standard deviations of spot-to-spot and sample-to-sample are down to 7.4% and 6.1%, respectively, suggesting an excellent reproducibility. We have further demonstrated the GNRs-GDMS as a SERS biosensor for detecting MGITC, melamine, and cytosine molecules with their detection limits of 10 nM, 100 nM, and 1 μM , respectively, which are better than some existing work with similar nanoparticles. Moreover, this GDMS-based concept is compatible with other sub-wavelength nanoparticles with different morphologies. These advantages suggest that the scheme of GDMS-enhanced Raman scattering offers new opportunities for low-cost and high-performance SERS-related detection in daily life.

Experimental

Polymethyl methacrylate (PMMA, MW: 350 000), polystyrene (PS), and tridecafluoro-1,1,2,2-tetrahydrooctyl-1-trichlorosilane (TFOCS) were purchased from Sigma-Aldrich. The positive photoresist (AR-P 3740) was purchased from Allresist. Materials for hard-PDMS (h-PDMS), including (7–8% vinylmethylsiloxane)-(dimethylsiloxane) copolymer, 1,3,5,7-tetramethylcyclotetrasiloxane, platinumdivinyltetramethyl-disiloxane and (25–30% methylhydrosiloxane)-(dimethylsiloxane) copolymer were purchased from Gelest. Sylgard 184 for soft-PDMS (s-PDMS) was purchased from Dow Corning. The gold nanorod suspension ($3 \times 10^{11}\text{ mL}^{-1}$) was purchased from NanoSeedz. Rhodamine 6G, malachite green isothiocyanate, melamine, and cytosine used as Raman analytes were purchased from Sigma-Aldrich.

Fabrication of the grating of photoresist

A layer of PMMA (about 50 nm) was spin-coated onto a quartz slide as an adhesion layer, followed by baking on a hot plate at $190\text{ }^\circ\text{C}$ for 2.5 minutes. Then, the positive photoresist was spin-coated on the PMMA layer, followed by baking at $95\text{ }^\circ\text{C}$ for 1.5 minutes. The substrate covered by the photoresist was thereafter subjected to an exposure under the interference pattern of two laser beams for about 60 seconds. After the exposure, the sample was immersed in the developer (NaOH solution, 0.125 mol L^{-1}) for 10 seconds, and then washed by deionized water.

Fabrication of the PDMS mold

An h-PDMS/s-PDMS composite stamp used as a mold in nanoimprinting was prepared by the soft lithography. Briefly, the as-prepared photoresist grating was placed in a vacuum desiccator, together with several drops of TFOCS. This process

ensured that the entire surface of the photoresist grating was covered by a monolayer of TFOCS molecules through siloxane bonding, which prevents the cured PDMS from sticking to the mold. For the preparation of h-PDMS, a mixture 3.4 g of (7–8% vinylmethylsiloxane)-(dimethylsiloxane) copolymer (VDT-731, Gelest), 0.1 g of 1,3,5,7-tetramethylcyclotetrasiloxane (SIT7900.0, Gelest) and 0.05 g of platinumdivinyltetramethyl-disiloxane (SIP6831.1, Gelest) was stirred and degassed for 5 minutes. 0.5 g of (25–30% methylhydrosiloxane)-(dimethylsiloxane) copolymer (HMS-301, Gelest) was then added into the mixture and stirred quickly. The final mixture was spin-coated onto the photoresist grating and baked at 70 °C for 20 min, after that a thin layer of h-PDMS with the complementary structure was formed on the photoresist. For the s-PDMS, 30 g of the base and 3 g of the curing agent (Sylgard 184, Dow Corning) were mixed and then poured onto the h-PDMS layer. After degassing for 30 minutes and curing at 70 °C for 4 hours, and finally, the h-PDMS/s-PDMS composite was formed, which was the PDMS stamp used in the following step.

Fabrication of the GNRs-GDMS

10 nm of titanium and 100 nm of gold was sequentially deposited on a quartz slide by magneto-sputtering. Then, the PS films with varying thicknesses were spin-coated onto the gold surface.

Then, the PDMS stamp was imprinted into the PS layer under a uniaxial compression (112 kPa) at 140 °C for 15 minutes. After cooling in air and removing the compression, the PDMS stamp was peeled to obtain the GDMS. The spacer thickness between grating and gold film can be calculated according to the invariance of the PS volume, which can be tuned by the spin-coating process.

The GNR suspension (3×10^{11} mL $^{-1}$) was centrifuged twice (8000 rpm, 10 minutes) to remove the redundant surfactant, and then dispersed in deionized water with the same volume. The as-prepared GDMS was treated by oxygen plasma etching for 30 seconds to make its surface hydrophilic and negatively charged. Then, 100 μ L of positively charged GNR suspension was added dropwise onto the GDMS. To evaporate the solution, the GDMS was heated in an oven at 55 °C for 1 hour and then rinsed by deionized water to remove the unattached GNRs. After drying under a nitrogen flow, the GNRs-GDMS with a monolayer of GNRs was formed at the edge of the drop. In the center of the drop, sparse GNRs were attached on the GDMS, which was used to analyse the SERS performance of GNRs-GDMS with sparse GNRs.

To prepared GNRs-GDMS with higher density GNRs, a certain amount of GNR suspension was centrifuged twice (8000 rpm, 10 minutes) and then dispersed in deionized water with a fifth of the volume. Then, the GDMS was also treated by oxygen plasma and 100 μ L of GNR suspension was added dropwise onto it. After solution evaporation, water rinse and nitrogen flow dry, the GNRs-GDMS with a multilayer of GNRs assembled at the edge of the drop was formed.

Characterization

The surface morphologies of all the samples were characterized with scanning electron microscopy (AURIGA, Zeiss). All the reflection and transmission spectra of GNRs-GDMSs were carried out using a spectrophotometer (Lambda 950, PerkinElmer). The reflection spectrum of the pure gold nanorods on a flat PS film is collected from a home-made micro-area optical measurement system, which is schematically shown in Fig. S10, ESI.† A white-light supercontinuum source (Super K, NKT Photonics) was used to generate a quasi-parallel light, which was illuminated on the sample. The reflected light was collected and analyzed using a spectrometer (iHR550, HORIBA). The Raman spectra were recorded using a Raman spectrometer (LamRAM HR, Horiba Scientific).

Raman measurements

The as-prepared GNRs-GDMS was treated by oxygen plasma etching for 30 seconds to make its surface hydrophilic, and then the samples were soaked in the solutions for 1 hour. After that, the sample was washed with deionized water to remove the unadsorbed molecules and finally dried by flowing nitrogen.

In the Raman measurements, the excitation was a laser with a wavelength of 633 nm and a power of 0.6 mW. A 100 \times objective (NA = 0.9) lens was used to focus the light on to the samples, and the diameter of the spot was found to be 2 μ m by the CCD. The Raman signal was collected in a backscattered fashion. The signal acquisition time was 10 seconds for R6G and MGITC. Due to the lower signal intensity, the acquisition time of melamine and cytosine was set to be 30 seconds. The acquisition process was cycled twice to remove the spike noise.

Conflicts of interest

The authors declare no competing financial interest.

Acknowledgements

The authors acknowledge the financial support from the National Natural Science foundation of China (91850106, 11574406, 11874436, 11504437, and 61604179), the Key project of the NSF of Guangdong Province (No. 2016A030311049), the Pearl River S&T Nova Program of Guangzhou (201806010147), and the Fundamental Research Funds for the Central Universities (No. 17lgpy07).

Notes and references

- J. Li, Y. Huang, Y. Ding, Z. Yang, S. Li, X. Zhou, F. Fan, W. Zhang, Z. Zhou, D. Wu, B. Ren, Z. Wang and Z. Tian, *Nature*, 2010, **464**, 392–395.
- A. Kim, S. J. Barcelo, R. S. Williams and Z. Li, *Anal. Chem.*, 2012, **84**, 9303–9309.

- 3 S. Yang, X. Dai, B. B. Stogin and T.-S. Wong, *Proc. Natl. Acad. Sci. U. S. A.*, 2016, **113**, 268–273.
- 4 C. Zhu, G. Meng, P. Zheng, Q. Huang, Z. Li, X. Hu, X. Wang, Z. Huang, F. Li and N. Wu, *Adv. Mater.*, 2016, **28**, 4871–4876.
- 5 L. Xu, Z. Lei, J. Li, C. Zong, C. J. Yang and B. Ren, *J. Am. Chem. Soc.*, 2015, **137**, 5149–5154.
- 6 S. Tian, O. Neumann, M. J. McClain, X. Yang, L. Zhou, C. Zhang, P. Nordlander and N. J. Halas, *Nano Lett.*, 2017, **17**, 5071–5077.
- 7 G. C. Schatz, M. A. Young and R. P. Van Duyne, *Top. Appl. Phys.*, 2006, **103**, 19–45.
- 8 W. E. Doering and S. Nie, *J. Phys. Chem. B*, 2002, **106**, 311–317.
- 9 H. Liang, Z. Li, W. Wang, Y. Wu and H. Xu, *Adv. Mater.*, 2009, **21**, 4614–4618.
- 10 X. Zhang, C. Niu, Y. Wang, S. Zhou and J. Liu, *Nanoscale*, 2014, **6**, 12618–12625.
- 11 J. H. Lee, M. H. You, G. H. Kim and J. M. Nam, *Nano Lett.*, 2014, **14**, 6217–6225.
- 12 J. Fang, S. Du, S. Lebedkin, Z. Li, R. Kruk, M. Kappes and H. Hahn, *Nano Lett.*, 2010, **10**, 5006–5013.
- 13 X. Xia, J. Zeng, B. McDearmon, Y. Zheng, Q. Li and Y. Xia, *Angew. Chem., Int. Ed.*, 2011, **50**, 12542–12546.
- 14 A. Ahmed and R. Gordon, *Nano Lett.*, 2012, **12**, 2625–2630.
- 15 M. Chirumamilla, A. Toma, A. Gopalakrishnan, G. Das, R. P. Zaccaria, R. Krahne, E. Rondanina, M. Leoncini, C. Liberale, F. D. Angelis and E. D. Fabrizio, *Adv. Mater.*, 2014, **26**, 2353–2358.
- 16 D. Wang, W. Zhu, Y. Chu and K. B. Crozier, *Adv. Mater.*, 2012, **24**, 4376–4380.
- 17 D. Wang, W. Zhu, M. D. Best, J. P. Camden and K. B. Crozier, *Nano Lett.*, 2013, **13**, 2194–2198.
- 18 A. Gopalakrishnan, M. Chirumamilla, F. D. Angelis, A. Toma, R. P. Zaccaria and R. Krahne, *ACS Nano*, 2014, **8**, 7986–7994.
- 19 Y. Shen, X. Z. Cheng, G. Z. Li, Q. Z. Zhu, Z. G. Chi, J. F. Wang and C. J. Jin, *Nanoscale Horiz.*, 2016, **1**, 290–297.
- 20 L. B. Zhong, J. Yin, Y. M. Zheng, Q. Liu, X. X. Cheng and F. H. Luo, *Anal. Chem.*, 2014, **86**, 6262–6267.
- 21 J. Li, D. Fattal and Z. Li, *Appl. Phys. Lett.*, 2009, **94**, 263114.
- 22 X. Xu, D. Hasan, L. Wang, S. Chakravarty, R. T. Chen, D. L. Fan and A. X. Wang, *Appl. Phys. Lett.*, 2012, **100**, 191114.
- 23 A. Liu, W. H. E. Hofmann and D. H. Bimberg, *IEEE J. Quantum Electron.*, 2015, **51**, 1–8.
- 24 D. Chanda, K. Shigeta, T. Truong, E. Lui, A. Mihi, M. Schulmerich, P. V. Braun, R. Bhargava and J. A. Rogers, *Nat. Commun.*, 2011, **2**, 479.
- 25 A. V. Guardado, A. Safaei, S. Modak, D. Franklin and D. Chanda, *Phys. Rev. Lett.*, 2014, **113**, 263902.
- 26 P. Wang, O. Liang, W. Zhang, T. Schroeder and Y.-H. Xie, *Adv. Mater.*, 2013, **25**, 4918–4924.
- 27 A. M. Michaels and L. Brus, *J. Phys. Chem. B*, 2000, **104**, 11965–11971.
- 28 M. Kang, J.-J. Kim, Y.-J. Oh, S.-G. Park and K.-H. Jeong, *Adv. Mater.*, 2014, **26**, 4510–4514.
- 29 A. Martín, A. Pescaglini, C. Schopf, V. Scardaci, R. Coull, L. Byrne and D. Iacopino, *J. Phys. Chem. C*, 2014, **118**, 13260–13267.
- 30 B. Yan, A. Thubagere, W. R. Premasiri, L. D. Ziegler, L. D. Negro and B. M. Reinhard, *ACS Nano*, 2009, **3**, 1190–1202.
- 31 A. Tao, F. Kim, C. Hess, J. Goldberger, R. R. He, Y. G. Sun, Y. N. Xia and P. D. Yang, *Nano Lett.*, 2003, **3**, 1229–1233.
- 32 S. Srivastava, R. Sinha and D. Roy, *Aquat. Toxicol.*, 2004, **66**, 319–329.
- 33 W. Leng and P. J. Vikesland, *Langmuir*, 2014, **30**, 8342–8349.
- 34 A. K. Hau, T. H. Kwan and P. K. Li, *J. Am. Soc. Nephrol.*, 2009, **20**, 245–250.
- 35 Y. Wu and Y. Zhang, *Food Chem. Toxicol.*, 2013, **56**, 325–335.
- 36 N. E. Mircescu, M. Oltean, V. Chiş and N. Leopold, *Vib. Spectrosc.*, 2012, **62**, 165–171.
- 37 A. Kaleem, M. Azmat, A. Sharma, G. Shen and X. Ding, *Food Chem.*, 2019, **277**, 624–631.
- 38 A. M. Giovannozzi, F. Rolle, M. Segà, M. C. Abete, D. Marchis and A. M. Rossi, *Food Chem.*, 2014, **159**, 250–256.
- 39 X. Zhang, X. Xiao, Z. Dai, W. Wu, X. Zhang, L. Fu and C. Jiang, *Nanoscale*, 2017, **9**, 3114–3120.
- 40 A. Barhoumi and N. J. Halas, *J. Am. Chem. Soc.*, 2010, **132**, 12792–12793.
- 41 S. S. Cortes and J. V. Garcia-Ramos, *J. Raman Spectrosc.*, 1992, **23**, 61–66.